

# Probing Intermediate Mass Black Holes in M87 through Multi-Wavelength Gravitational Wave Observations

Razieh Emami and Abraham Loeb

*Center for Astrophysics, Harvard-Smithsonian, 60 Garden Street, Cambridge, MA 02138, USA*

Accepted XXX. Received YYY; in original form ZZZ

## ABSTRACT

We analyze triple systems composed of the super massive black hole (SMBH) near the center of M87 and a pair of black holes (BHs) with masses in the range  $10 - 10^3 M_{\odot}$ . We consider the post Newtonian precession as well as the Kozai-Lidov interactions at the quadruple and octupole levels in modeling the evolution of binary black hole (BBH) under the influence of the SMBH. Kozai-Lidov oscillations enhance the gravitational wave (GW) signal in some portions of the parameter space. We identify frequency peaks and examine the detectability of GWs with LISA as well as future observatories such as  $\mu$ Ares and DECIGO. We show examples in which GW signal can be observed with a few or all of these detectors. Multi-Wavelength GW spectroscopy holds the potential to discover stellar to intermediate mass BHs near the center of M87. We estimate the rate,  $\Gamma$ , of collisions between the BBHs and flyby stars at the center of M87. Our calculation suggest  $\Gamma < 10 \text{ Gyr}^{-1}$  for a wide range of the mass and semi-major axes of the inner binary.

**Key words:** Gravitational Waves, Intermediate Mass BHs, M87

## 1 INTRODUCTION

Black holes (BHs) are ubiquitous in galaxies and form across a wide range of masses and environments. Stellar-mass BHs are most abundant, with observational evidence first detected in X-rays (Webster & Murdin 1972; Remillard & McClintock 2006), and more recently by gravitational waves (GWs) with LIGO/Virgo (Abbott et al. 2016a,b). Intermediate mass black holes (IMBHs) are expected to form from the accretion of gas in dwarf galaxies (see (Reines et al. 2019) and references therein), mergers of stars in dense stellar clusters (Portegies Zwart et al. 1999; Devecchi & Volonteri 2009; Pan & Loeb 2012; Mapelli 2016), from direct collapse of inflowing dense gas in protogalaxies (Loeb & Rasio 1994), collapse of Pop III stars from early universe (Madau & Rees 2001; Bromm & Larson 2004), from supermassive stars in AGN accretion disk instabilities (McKernan et al. 2012, 2014) or as recently proposed by Giersz et al. (2015) a consequence of dynamical interaction between hard binaries, containing stellar mass BH, and other stars and binaries.

Finding unambiguous observational evidence for IMBH candidates in galactic nuclei is challenging due to the short lifetime associated with mergers and accretion by the supermassive black holes (SMBHs) there (Natarajan 2014; Johnson & Haardt 2016). There is however some evidence for their existence in the local Universe (Mezcua 2017). In particular, Ultraluminous X-ray sources (ULXs) imply BHs

with masses above  $20 M_{\odot}$  in some cases (Miller & Colbert 2004). A recent discovery of IMBH candidates in dwarf galaxies at ( $z \lesssim 2.4$ ) was reported in the Chandra COSMOS Legacy Survey (Mezcua et al. 2018), using a sample of 40 active galactic nuclei (AGN) in dwarf galaxies with redshift below 2.4. More recently (Chilingarian et al. 2018) used data mining in wide-field sky surveys and identified a sample of 305 IMBH candidates in galaxy centers, accreting gas which creates characteristic signatures of a type I AGN. Most recently, a new sample of Wandering IMBH was discovered using the large-scale and high resolution radio telescopes (Reines et al. 2019) in nearby dwarf galaxies.

New probe of IMBH candidates are awaited using 30-m class telescopes (Greene et al. 2019). IMBH candidates may also be able to detect using the GW signals in different frequencies (Kocsis & Levin 2012).

SMBHs, with masses in the range  $10^6 - 10^{10} M_{\odot}$  are believed to exist in the core of almost all of massive galaxies (Wang et al. 2015; Broderick et al. 2015). This includes SgrA\* at the Galactic center (Ghez et al. 1998; Gravity Collaboration et al. 2018), as well as the nearby elliptical galaxy M87 (Gebhardt & Thomas 2009; Gebhardt et al. 2011; Walsh et al. 2013). Most recently the mass of the M87 SMBH was precisely measured by Event Horizon Telescope (EHT) collaboration (Event Horizon Telescope Collaboration et al. 2019a,b,c,d,e,f) to be  $6.5 \times 10^9 M_{\odot}$ . In addition to the above constraints on the mass of M87, there are some

studies on the proper motion and core stability in Virgo cluster. Walker et al. (2009) monitored the relative position of M87 and M84 at 43 GHz with the Very Long Baseline Array Astrometry (VLBA). This study demonstrated a 5 sigma detection of a relative motion 800 km/s.

Being at the center of the virgo cluster, M87 is the nearest giant elliptical galaxy which is the product of many galaxy mergers. As a result, M87 should contain a large population of stellar mass BHs and possibly a handful of IMBH candidates which used to be at the center of dwarf galaxies that merged in. Here we propose to search for this IMBH populations in M87 through their GW signals.

A large fraction of the IMBH candidates in M87 might result in binaries in eccentric orbits around the SMBH. This system is well described by the hierarchical triple approach (Naoz et al. 2013; Grishin et al. 2017, 2018; Randall & Xianyu 2019; Hoang et al. 2019; Antonini et al. 2019) in which the inner binary contains of IMBH candidates while the outer binary includes the SMBH. The IMBH candidates in the inner binary are expected to emit bursts of GWs at any pericenter passage. The frequency of these GW bursts depend on the orbital parameters.

In this paper, we simulate triple systems composed of M87 and a pair of the BHs and consider the dynamical evolution of the binary BHs. The induced Kozai-Lidov oscillations (Naoz et al. 2013; Antonini et al. 2018; Rodriguez & Antonini 2018; Randall & Xianyu 2019; Hoang et al. 2019; Antonini et al. 2019) are ubiquitous for low mass BHs. Increasing the mass of BHs in the binary suppresses the strength of the Kozai-Lidov oscillations. We present examples in which the GW signal is above the noise of future observatories, including LISA (Robson et al. 2019; Emami & Loeb 2019),  $\mu$ -Ares (Sesana et al. 2019), a newly proposed space based GW mission with the ability of filling the gap between the milli-Hz and nano-Hz frequency windows surveyed by LISA, and also Decihertz Observatories (DOs) such as the Decihertz Interferometer GW observatory (DECIGO) (e.g. Arca Sedda et al. (2019) and Refs. in this). Adapting a maximum observational time of up to 10 yrs, we present examples with detectable GW signals by these observatories.

The paper is organized as follows. In Sec. 2 we briefly review the details of the related hierarchical triple system. In Sec. 3 we introduce the stability conditions that must be taken into account. In 4.1 we review the finite time Fourier transformation for computing the GW signal. In Sec. 4.2 we present a variety of different examples with a potentially detectable GW signal as demonstrated in Sec. 5. In Sec. 6 we briefly consider binaries with non-equal BH masses. In Sec. 7 we estimate the rate of collision between the inner BBH and the flyby stars. In Sec. 8 we compute the lifetime of the related systems. we discuss about the detectability of the GW signal. Finally, we summarize our conclusions in Sec. 9.

## 2 IMPACT OF SMBH ON THE EVOLUTION OF BBHS

We model the dynamical influence of a SMBH on the evolution of BBHs, accounting for inner pericenter precession at first order, quadruple and octupole terms in the Lidov-Kozai interaction.

The full Hamiltonian of the triple system is given by,

$$H_{tot} = H_{LK} + H_{1PN}, \quad (1)$$

where  $H_{LK}$  and  $H_{1PN}$  present the Lidov-Kozai Hamiltonian and first order post Newtonian precession, respectively.  $H_{LK} = H_1 + H_2 + H_{12}$  with  $H_i, i = 1, 2$  referring to the Keplerian Hamiltonian for the inner and outer binaries in the system and  $H_{1,2}$  denoting the interaction term between them. The interaction term is expressed as a series expansion in the separation of two binaries. We make use of Eqs. (5-8) of Antonini et al. (2018); Rodriguez & Antonini (2018) for modeling the above components of full Hamiltonian.

Using Eq. (1) we derive the equations of motion for the inner and outer semi-major axes. We also take into account GW emission in the inner orbit as an extra term that shrinks the orbit of the BHs.

## 3 STABILITY CONDITIONS

Here we present some stability conditions that must be taken into account in our analysis:

- The orbital parameters must be selected such that prevent the inner binary from reaching the Roche limit of the outer-binary (Hoang et al. 2018; Fragione et al. 2019). This implies,

$$\frac{a_{out}}{a_{in}} > \left( \frac{1 + e_{in}}{1 - e_{out}} \right) \left( \frac{3M_{SMBH}}{m_1 + m_2} \right)^{1/3}. \quad (2)$$

The above widely used analytical stability criteria does not account for possible changes in the Hill radius due to the inclination (Grishin et al. 2017). However, as it was demonstrated in (Grishin et al. 2017), the numerical fit gives us an excellent agreement to the analytical expression up to 120 degree and a marginal agreement afterward.

- The system must possess dynamical stability, implying that the hierarchical secular treatment is satisfied (Naoz & Silk 2014; Hoang et al. 2018),

$$\left( \frac{a_{in}}{a_{out}} \right) \left( \frac{e_{out}}{1 - e_{out}^2} \right) < 0.1. \quad (3)$$

- For eccentric outer orbits, we add one extra criteria for the pericenter of the outer orbit. We urge the pericenter distance to be relatively larger than the event horizon of SMBH,

$$a_{out} (1 - e_{out}) > 2 \left( \frac{GM_{SMBH}}{c^2} \right). \quad (4)$$

This criteria makes us ensure that the outer orbit does not hit the event horizon of the SMBH. This is expected as otherwise we lose the outer binary at the first pericenter crossing. While this criteria is easier to achieve for moderately massive SMBH, such as SgrA\*, it needs to be checked for a massive SMBH like M87.

## 4 GRAVITATIONAL WAVES ESTIMATION

Given the dynamical evolution of the orbital parameters, we calculate the GW amplitude from eccentric binary black

holes (hereafter EBBHs) and study the detectability of their GW signal. Using this formalism, we present some examples with potentially detectable GW signals in M87.

#### 4.1 GW-Computation

Unlike binaries on circular orbits, EBBHs emit GW in a discrete spectrum (Peters & Mathews 1963) with characteristic frequencies  $f_n = n f_{\text{orb}}$ , where  $n$  refers to the harmonic index while  $f_{\text{orb}} = (2\pi)^{-1} \sqrt{G(m_1 + m_2)a^{-3/2}}$  is the orbital frequency in a circular orbit with semi-major  $a$  and  $m_1$  and  $m_2$  refer to the mass of BHs in the inner binary. The amplitude of the GW signal is given by,

$$h(a, e, t) = \sum_{n=1}^{\infty} h_n(a, e, f_n) \exp(2\pi i f_n t), \quad (5)$$

where  $h_n(a, e, f_n)$  is defined as,

$$h_n(a, e, f_n) = \frac{2}{n} \sqrt{g(n, e)} h_0(a), \quad (6)$$

with  $h_0(a)$  being the dimensionless strain for a circular orbit, given by (Peters & Mathews 1963; Randall & Xianyu 2019; Hoang et al. 2019),

$$h_0(a) = \sqrt{\frac{32}{5}} \frac{G^2}{c^4} \frac{m_1 m_2}{D a}, \quad (7)$$

and where  $D$  denotes the angular diameter distance to the source.

To gauge the detectability of the GW signal, we divide the stream of GW into time intervals with a duration  $\Delta T$  and perform a Finite Fourier Transformation (FFT) of the GW strength for the duration  $\Delta T$ . The Fourier component of the GW signal can be computed by taking a time integral of Eq. (5) from  $-(\Delta T/2)$  to  $(\Delta T/2)$  yielding,

$$\tilde{h}(a, e, f) = \sum_{n=1}^{\infty} h_n(a, e, f_n) \Delta T w(f, f_n, \Delta T), \quad (8)$$

where,

$$w(f, f_n, \Delta T) = \frac{\sin[\pi(f - f_n)\Delta T]}{\pi(f - f_n)\Delta T}. \quad (9)$$

The observational interval  $\Delta T$  plays an important role. For close-in sources, the strength of GW is large enough to allow smaller values of  $\Delta T$ . This leads to wider frequency bins, as  $f - f_n \simeq 1/\Delta T$ . The situation is different for wide-separation binary systems, where the observational time  $\Delta T$  must be larger. Therefore the GW signal is localized in the frequency domain around specific harmonics. We define *characteristic* detectable frequencies which are aimed to be within the frequency range of LISA or ground based GW detectors,

$$f_{\min} \leq f \equiv f_n \pm \alpha/\Delta T \leq f_{\max}, \quad (10)$$

where  $\alpha \lesssim 1$  and with  $f_n = n f_{\text{orb}}$ .

Next, we define the characteristic strain of the GW signal as,

$$h_c^2(a, e, f) \equiv 4f^2 |\tilde{h}(a, e, f)|^2. \quad (11)$$

To check the detectability of the GW signal, Eq. (11) must

be compared with the characteristic noise of GW observatories. As discussed in the introduction, we will consider several different GW detectors, including LISA,  $\mu$ -Ares and DECIGO.

Defining the noise generically as  $S_c(f)$ , the signal to noise ratio (S/N) is given by,

$$(S/N)^2(a, e) = \int_{f_{\min}}^{f_{\max}} \frac{h_c^2(a, e, f)}{S_c(f)} d(\ln f). \quad (12)$$

#### 4.2 GW signal in M87

Having presented a formalism to compute the GW signal for a generic system, we now apply it to the case of M87. Since  $D = 16\text{Mpc}$ , we choose a relatively large value for the observational time,  $\Delta T$ . From Eq. (8), a large  $\Delta T$  has two different effects, though. On the one hand, it enhances the GW amplitude. On the other hand, it diminishes the frequency width of the GW signal as  $(f - f_n) \simeq 1/\Delta T$ . This leads to a discrete spectrum of observable frequencies. The combination of these two effects lead to a range of  $\Delta T$  that can lead to an observable GW signal at a range of discrete frequencies.

To clarify the above points, we present some examples with potentially detectable GW signals at different frequencies. We choose  $\Delta T$  differently in each of these examples to both help pushing the GW signals above the noise as well as increasing the amount of observable frequencies.

Throughout our analysis, we neglect the GW bursts from the inspiral phase of IMBH around M87. In another paper (Emami & Loeb 2019), we estimated the timescale associated with these bursts to be,

$$\tau_{\text{GW}} \simeq \left(\frac{5}{64}\right) \frac{c^5 a_{\text{out}}^4 (1 - e_{\text{out}}^2)^{7/2}}{G^3 (m_1 + m_2) M_{87}^2} \left(1 + \frac{73}{24} e_{\text{out}}^2 + \frac{37}{96} e_{\text{out}}^4\right)^{-1}. \quad (13)$$

It is easy to see that  $\tau_{\text{GW}} \simeq \mathcal{O}(\text{Gyr})$  is much longer than both of the observational time and the lifetime of the orbit of IMBH. Therefore, we can safely ignore the GW decay time in our analysis.

##### 4.2.1 Probing GW in LISA

First, we consider GWs in the LISA band. We adopt the LISA noise curve (Robson et al. 2019; Emami & Loeb 2019) and present the characteristic GW signal on the top of that. Figure 1 shows the GW signal in the LISA band for few different equal mass binaries with each component having,  $\tilde{m} (\equiv m/M_{\odot}) = (10, 50, 100, 300, 500, 700, 1000)$ . The rest of the parameters are chosen to be the same:  $\tilde{a}_{\text{in}} = 0.05, \tilde{a}_{\text{out}} = 4000, e_{\text{in}} = 0.7, e_{\text{out}} = 0.7$ , where hereafter  $\tilde{a} \equiv (a/\text{AU})$ . On the left panel, we use an interpolation for the points with  $\pi(f - f_n)\Delta T < 1$ , whereas the right panel, presents the points satisfying  $\pi(f - f_n)\Delta T < 1$ . We adopt  $\Delta T = (8, 7, 5, 2, 1, 0.5, 0.5)$  yrs.

##### 4.2.2 Probing GW with the $\mu$ -Ares detector

Since the LISA noise increases at frequencies below milli-Hz, it is advantageous to use the newly proposed  $\mu$ -Ares

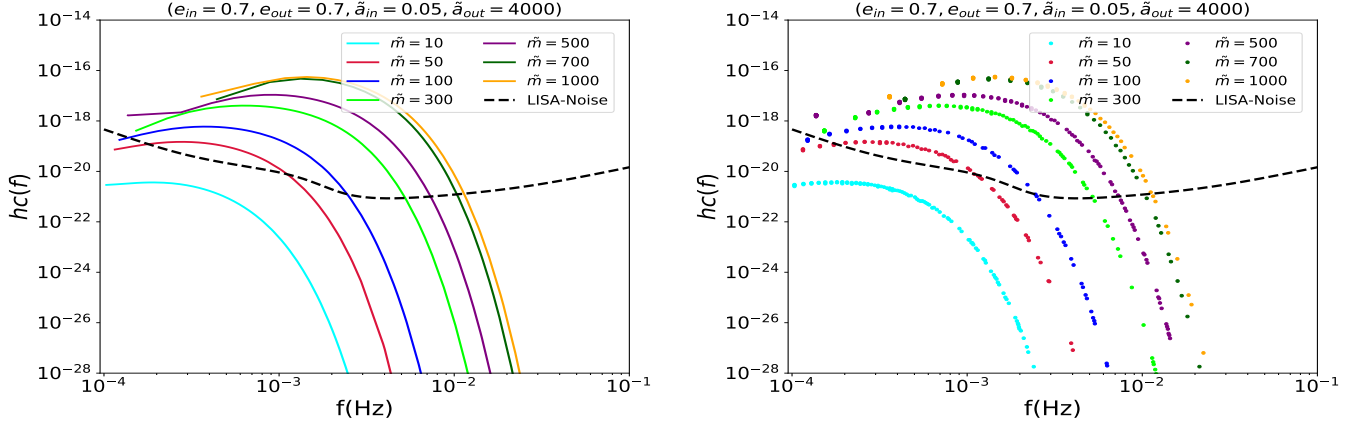


**Figure 1.** GW signal (in color) relative to the LISA noise (dashed black line) for equal mass binaries with individual masses  $\tilde{m} \equiv m/M_{\odot} = (10, 50, 100, 300, 500, 700, 1000)$ . Left: the interpolated GW signal with  $\pi(f - f_n)\Delta T < 1$ . Right: discrete frequencies with the above condition. The Signal to Noise ratio for LISA in the above examples is  $S/N = (0.1, 0.8, 5.7, 82, 224)$ , respectively.

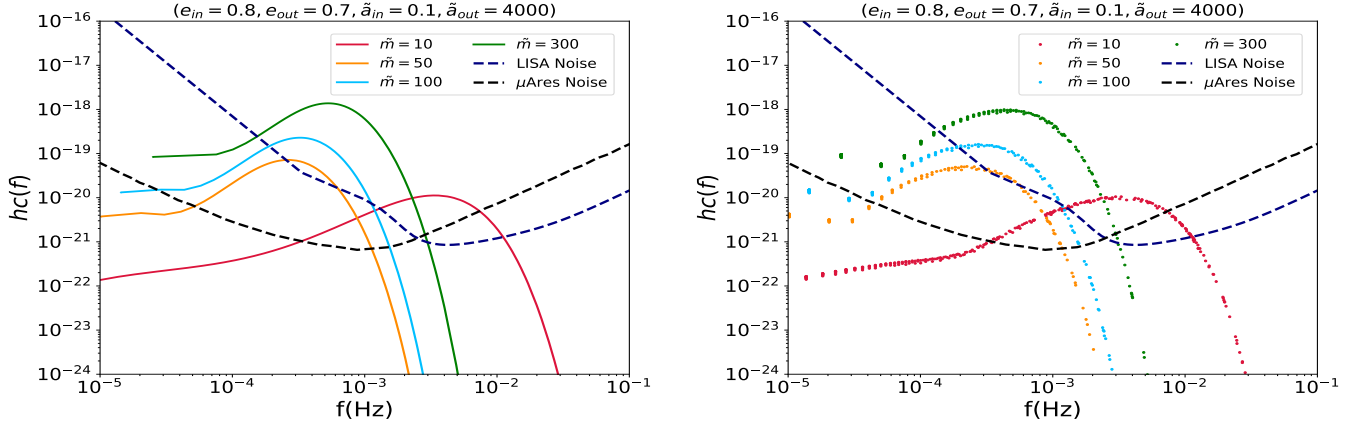


**Figure 2.** GW signal (in color) compared to  $\mu$ -Ares (dashed blue) and LISA noise (dashed black) for BBHs with individual mass  $\tilde{m} = (10, 50, 100, 300)$ . Left: the interpolated GW signal with  $\pi(f - f_n)\Delta T < 1$ . Right: discrete frequencies with the above condition. Signal to Noise ratios for the  $\mu$ -Ares examples are  $S/N = (91, 266, 947, 7.5 \times 10^3)$ .

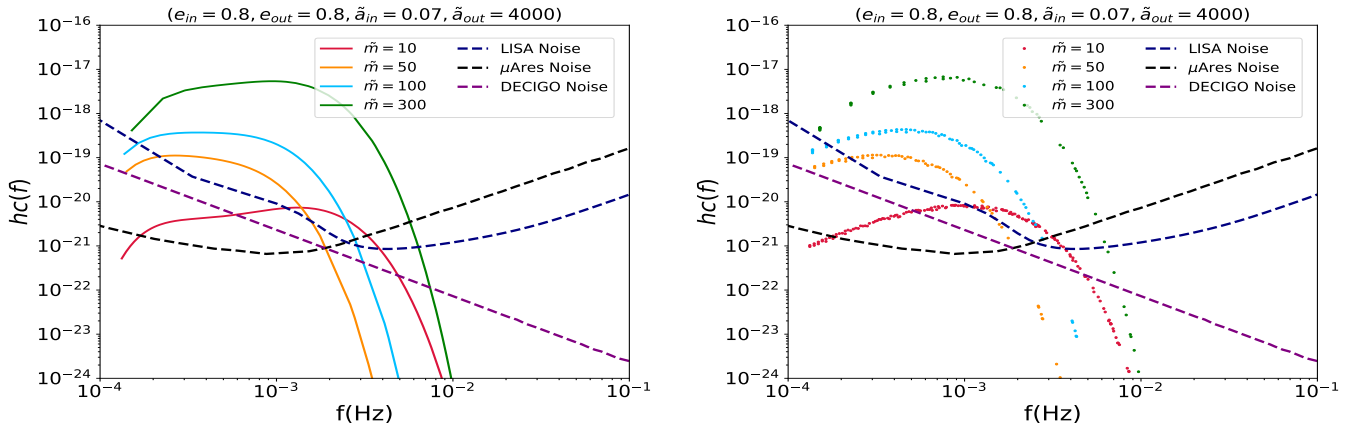


**Figure 3.** GW signal (in color) compared to LISA (dashed blue),  $\mu$ -Ares (dashed black) and DECIGO (dashed purple) noises for BBHs with individual mass  $\tilde{m} = (10, 50, 100, 300)$ . Left: the interpolated GW signal with  $\pi(f - f_n)\Delta T < 1$ . Right: discrete frequencies with the above condition. Signal to Noise ratio for DECIGO are given by  $S/N = (52, 100, 560, 1.44 \times 10^4)$ .

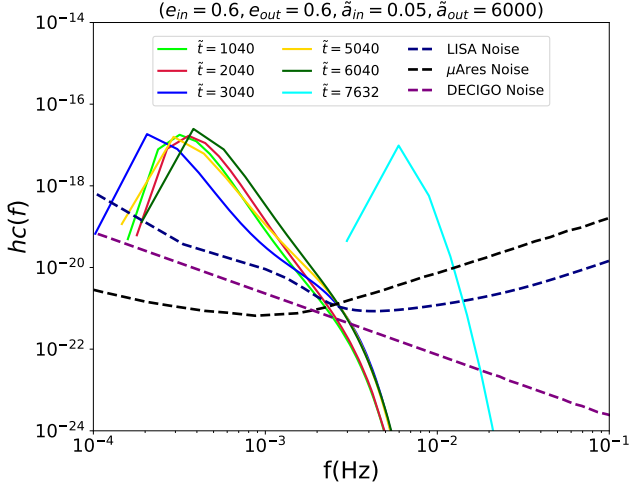


**Figure 4.** The time evolution of the GW signal over a wide range of frequencies. We have taken  $\tilde{t} = (1040, 2040, 3040, 5040, 6040, 7632)$ , where  $\tilde{t} \equiv (t/\text{yr})$ , and  $\Delta T = (9, 8, 6, 5, 4, 0.1)\text{month}$ .

detectors for detecting GW signals in the frequency range from  $\mu\text{Hz}$  to milli-Hz. Figure 2 presents the characteristic strength of GW at those frequencies. For BH masses with  $\tilde{m} = (10, 50, 100, 300)$ . The plot is shown for  $\tilde{a}_{in} = 0.1, \tilde{a}_{out} = 4000, e_{in} = 0.8, e_{out} = 0.7$ . Comparing Figure 2 with Figure 1, reveals that the strength of GW for  $\tilde{m} = 10$  is enhanced for larger value of inner semi-major axes. This is due to the Kozai-Lidov oscillations which boost the GW signal above the noise toward larger frequencies. Here we consider  $\Delta T = (10, 8, 5, 2)$  yrs.

#### 4.2.3 Probing GW with Decihertz Observatories (DOs)

Finally, we consider decihertz frequencies,  $f \sim (0.01 - 1)$  Hz, which are particularly suitable to IMBHs (Arca Sedda et al. 2019). There are currently different proposed technologies for probing the GWs within this frequency range. They include DO-optimal, DO-conservative, Advanced Laser Interferometer Antenna (ALIA) and decihertz Interferometer GW observatory (DECIGO) (see, e.g. Arca Sedda et al. (2019) and Refs. therein). In our analysis below, we focus on DECIGO. Figure 3 presents the characteristic GW strain against various detectors including the LISA (blue line),  $\mu\text{Ares}$  (black line) and DECIGO (purple line) for  $\Delta T = (10, 8, 5, 3)$  yrs.

There are clearly overlapping regions in frequency for these three observatories. This is particularly helpful in removing degeneracies between various parameters in the system. Multi-wavelength spectroscopy of GW can provide novel information about the parameters of the BBHs that are otherwise degenerate, and could be potentially used as a way to discover IMBHs in M87.

#### 4.2.4 Time evolution of GW amplitude

Having presented the frequency evolution of the GW signal for a fixed time, we next study how the signal changes with time. In Figure 4, we draw the evolved

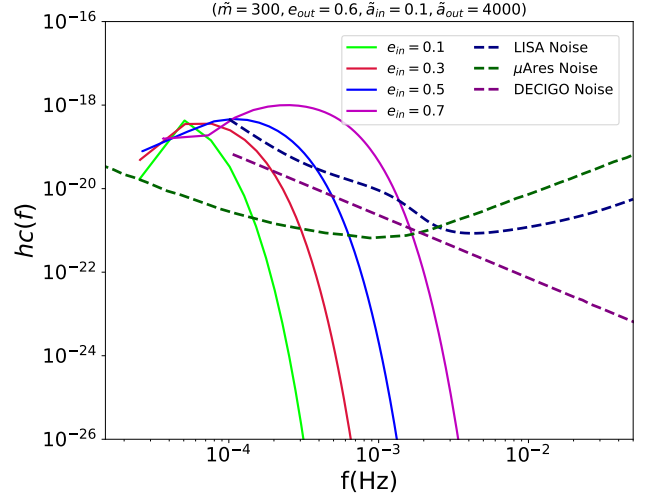


**Figure 5.** The dependence of the GW signal on  $e_{in} = (0.1, 0.3, 0.5, 0.7)$ ,  $\tilde{m} = 300, e_{out} = 0.6, \tilde{a}_{in} = 0.1, \tilde{a}_{out} = 4000$ , and  $\Delta T = 2\text{yrs}$ .

GW in a wide range of frequencies. Here we adopt  $\tilde{m} = 300, e_{in} = 0.6, e_{out} = 0.6, \tilde{a}_{in} = 0.05, \tilde{a}_{out} = 6000$ . We consider  $\tilde{t} = (1040, 2040, 3040, 5040, 6040, 7632)$  for  $\Delta T = (9, 8, 6, 5, 4, 0.1)$  month. In this example, increasing  $\Delta T$  mostly affects the detectability of the GW signal for the DECIGO observatory.

#### 4.2.5 Impact of orbital parameters in GW amplitude

In our simulations, we fix some of the orbital parameters such as the arguments of pericenter for the inner and outer binaries (taken to be  $0^\circ$ ), longitude of ascending node for inner and outer binaries (chosen to be  $0^\circ$ ) and mutual inclination (taken to be  $90^\circ$ ). We have also taken the BHs to have zero spins, but allowed rest of the parameters to vary. This includes the inner and outer semi-major axes and eccentricities. We noticed that changing the outer semi-major axis has very minor impact on the results as long as the BBH is far from the tidal disruption distance,  $a_{out} \gg a_{in}(M_{SMBH}/M_{BH})^{1/3}$ . Similarly, changing  $e_{out}$  does not affect the signal significantly. On the other hand, changing  $a_{in}$  and especially  $e_{in}$  affect the strength of the signal dramatically. Owing to the importance of these parameters, we consider their effect on the GW signal for multiple detectors.

Figure 5 presents the influence of  $e_{in}$  on the GW signal, assuming  $\tilde{m} = 300, e_{out} = 0.6, \tilde{a}_{in} = 0.1$  and  $\tilde{a}_{out} = 4000$ . The resulting GW signal could be observed by  $\mu\text{Ares}$ , LISA or DECIGO detectors.

Finally, in Figure 6 we examine the impact of changing  $\tilde{a}_{in} = (0.03, 0.05, 0.07, 0.1, 0.15, 0.2)$  on the detectability of GW signal. Here we adopt  $\tilde{m} = 300, e_{in} = 0.7, e_{out} = 0.6, \tilde{a}_{out} = 6000$ . The plot shows that changing  $a_{in}$  only affects slightly the GW signal.



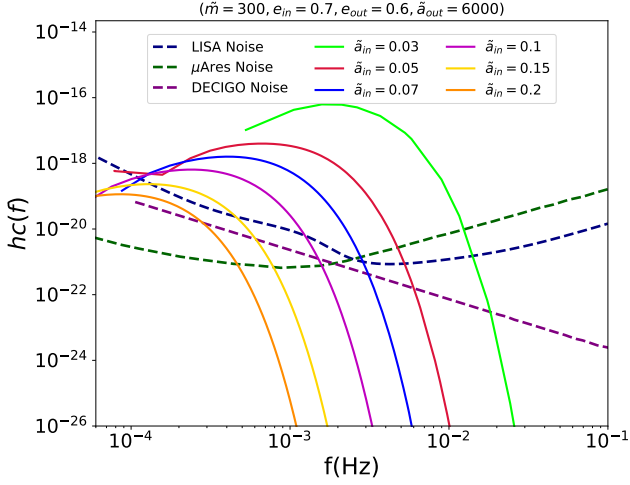


**Figure 6.** The dependence of the GW signal on  $\tilde{a}_{in} = (0.03, 0.05, 0.07, 0.1, 0.15, 0.2)$ , for  $\tilde{m} = 300$ ,  $e_{in} = 0.7$ ,  $e_{out} = 0.6$ ,  $\tilde{a}_{out} = 6000$ , and  $\Delta T = 2$  yrs.

**Table 1.** Frequency band for different GW observatories.

Detector	$f_{min}(\text{Hz})$	$f_{max}(\text{Hz})$
$\mu\text{Ares}$	$\max(10^{-6}, f_m)$	$10^{-3}$
LISA	$f_m$	$10^{-1}$
DECIGO	$10^{-3}$	10

## 5 DETECTABILITY OF GW SIGNAL

Next, we consider the detectability of GW signals for some of the examples above. We compute the signal to noise ratio (S/N) using Eq. (12), and label a GW signal as detectable if  $S/N \geq 10$ . The exact lower limit in  $S/N$  is not fixed. Different values are used in the literature. For example [Hoang et al. \(2019\)](#) used  $S/N \geq 5$  as the criteria of detection. Here we use a more conservative criteria of 10 as our detection limit. Since different GW detectors are focused on different frequency bands, we need to define the frequency bands for different detectors using Eq. (12). Table 1 presents the frequency ranges for different GW detectors. Although for most cases we take the universal upper and lower limits in the integrals, the lower limit for  $\mu\text{Ares}$  depends on the minimum value of the frequency, which could be slightly larger than  $10^{-6}\text{Hz}$ . Owing to this, we take the maximum value between  $10^{-6}\text{Hz}$  and  $f_m$ , defined to be the minimum value of the frequency of GW signal. Likewise, for the LISA experiment, we take the minimum value of the frequency of signal as the lower limit of the integral.

In addition, since the GW frequency is chirped towards the merger, the computation of the SN also depends on the approximate point in the evolution of the system. In other words, the time evolution of the system affects the GW signal and so the S/N. Therefore, lower signal to noise may evolve with time and get enhanced. With this in our mind, in the following we present S/N ratio for one set of the examples. Table 2 presents the signal to noise ratio for

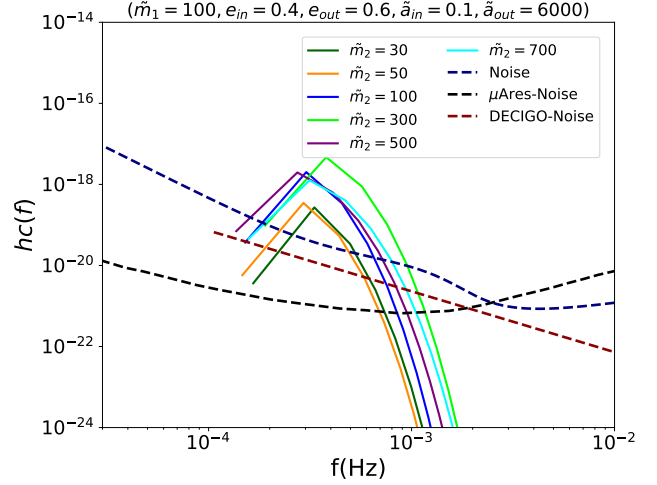


**Figure 7.** GW signal for non-equal BH masses. Here we adopt  $m_1 = 100M_\odot$  and consider different values for its companion mass in the range  $m_2 = (30, 50, 100, 300, 500, 700)M_\odot$ . The remaining orbital parameters are taken to be  $a_{in} = 0.1\text{AU}$ ,  $e_{in} = 0.4$ ,  $e_{out} = 0.6$ ,  $a_{out} = 6000\text{AU}$ .

the case with  $\tilde{m} \equiv m/M_\odot = (10, 50, 100, 300, 500, 700, 1000)$  and with  $\tilde{a}_{in} = 0.1$ ,  $\tilde{a}_{out} = 4000$ ,  $e_{in} = 0.8$ ,  $e_{out} = 0.7$ , and  $\Delta T = (9, 8, 5, 3, 2, 1, 1, 1)\text{yr}$ . The GW signal is evaluated at the same time for all cases. Since the dynamical evolution of different BHs differ depending on their masses, the orbital and peak frequency,

$$f_p = 2f_{orb} \frac{(1 + e_{in})^{1.1954}}{(1 - e_{in}^2)^{3/2}}, \quad (14)$$

is different in these examples. Therefore over the time, the location of signal changes for different BH masses and we may put them in the same location if we look at individual ones at different times.

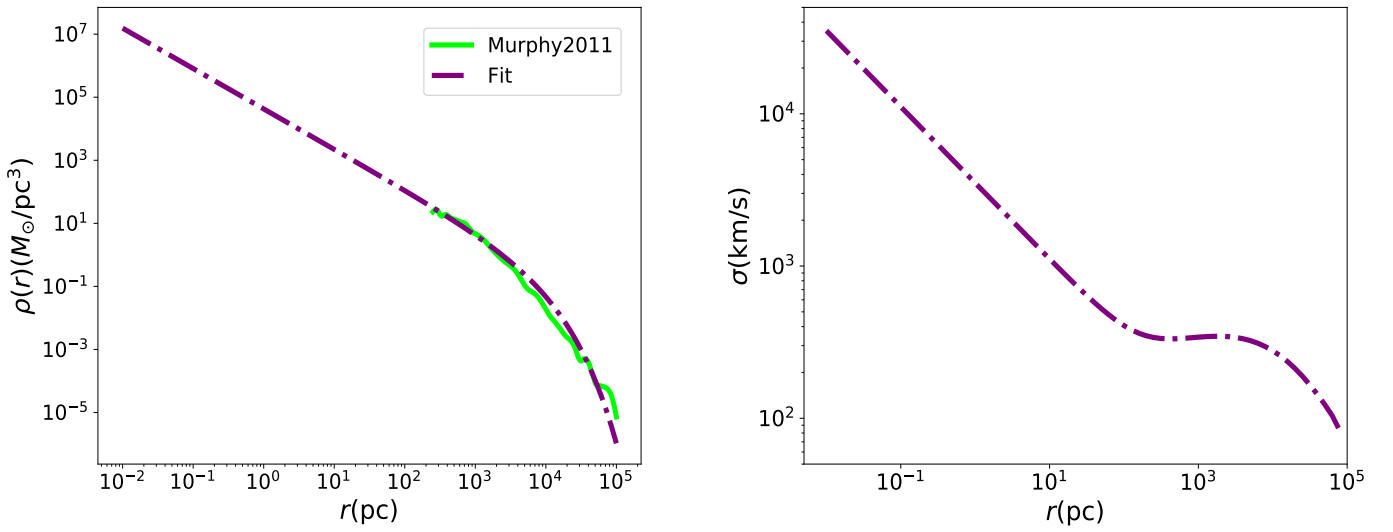
## 6 NON-EQUAL MASS BHs

So far, we only focused on the BBHs with equal masses. Here we briefly consider the case with non-equal BH masses. As a test example, we fix the mass of one of BHs to be  $m_1 = 100M_\odot$  and change the mass of its companion in the range  $m_2 = (30, 50, 100, 300, 500, 700)M_\odot$ . The rest of the orbital parameters are taken to be  $a_{in} = 0.1\text{AU}$ ,  $e_{in} = 0.4$ ,  $e_{out} = 0.6$ ,  $a_{out} = 6000\text{AU}$ . Figure 7 presents the GW signal for this regime.

Unlike the examples in Sec. 5, we evaluate the GW signal at the time for which the peak frequency (defined in Eq. 14) to be around  $f_p = 3 \times 10^{-4}\text{Hz}$ . This makes the GW signal behave very similarly. Therefore the peak frequency is a key parameter in our system and leads to an almost universal behavior at different BH masses. In closing, we note that each IMBH may carry a cluster of stellar-mass BHs around it, enhancing the rate of detectable GW signals from its vicinity.

**Table 2.** Signal to Noise (S/N) ratio for different BH masses and with  $\tilde{a}_{in} = 0.1$ ,  $\tilde{a}_{out} = 4000$ ,  $e_{in} = 0.8$ ,  $e_{out} = 0.7$ .

BH mass ( $M_\odot$ )	$\mu$ Ares	LISA	DECIGO
10	3.6	9.4	38.5
50	41.1	1.2	0.3
100	148	4.8	2.6
300	$1.7 \times 10^3$	86	163
500	$4.3 \times 10^3$	$3.2 \times 10^2$	793
700	$5.5 \times 10^3$	$5.45 \times 10^2$	$1.4 \times 10^3$
1000	$1.6 \times 10^4$	$2.5 \times 10^3$	$6.7 \times 10^3$


**Figure 8.** Density profile (left) and velocity dispersion (right) of M87.

## 7 INTERACTION BETWEEN BBH AND FLYBYS

So far we considered the impact of the SMBH on the evolution of BBHs at M87 and its imprint on gravitational waves. We ignored the impact of any flybys in the evolution of system. Since M87 is surrounded by a stellar cluster, there might be some flyby stars that reach BBHs. It is therefore intriguing to have an order of magnitude estimation on the rate of collisions leaving its comprehensive study for a future paper.

The rate of different collisions and dynamical interactions in galactic nuclei and globular clusters have been considered in [Leigh et al. \(2016, 2014, 2018\)](#). Following [Leigh et al. \(2018\)](#), we compute the rate of interaction between an inner BBH and a cloud of stars belonging to the stellar cluster around M87. We ignore the impact of the stellar disk and focus on the dispersion supported spherical stellar component of M87. The rate of collisions between the inner BBH and stars is given by [Leigh et al. \(2018\)](#),

$$\Gamma \simeq \rho(r) \left( \frac{R^2}{M} \right) \left( 1 + \left( \frac{v_e}{\sigma(r)} \right)^2 \right) \sigma(r), \quad (15)$$

where  $\rho(r)$  and  $\sigma(r)$  describe to the mass density of dispersion supported stellar component and velocity dispersion next to SMBH with  $r$  referring to the distance from the central SMBH. Here,  $v_e = \left( \frac{2GM}{R} \right)^{1/2}$  describes the escape velocity from the BBH. Finally, in the above formula we take  $M$  and  $R$  to be the mass of BBH as well as the semi-major of orbit, respectively.

For the density profile,  $\rho(r)$ , we use Figure 9 of [Murphy et al. \(2011\)](#) to infer the total enclosed mass of stars at every radius  $r$  from M87. Density profile can then be computed from the derivative of the enclosed mass. We fit a non-linear function to the density profile and extend it to smaller radii above the data resolution. The left panel in Figure 8 presents the density profile of M87 for [Murphy et al. \(2011\)](#) and our non-linear fit.

Using the above extended mass/density profiles, we next compute the velocity dispersion as,

$$\sigma^2(r) = \left( \frac{G}{\rho(r)} \right) \int_r^\infty \left( \frac{\rho(r')}{r'^2} \right) \left( M_{SMBH} + M_\star(r') \right) dr', \quad (16)$$

The right panel in Figure 8 displays the radial profile of the velocity dispersion.

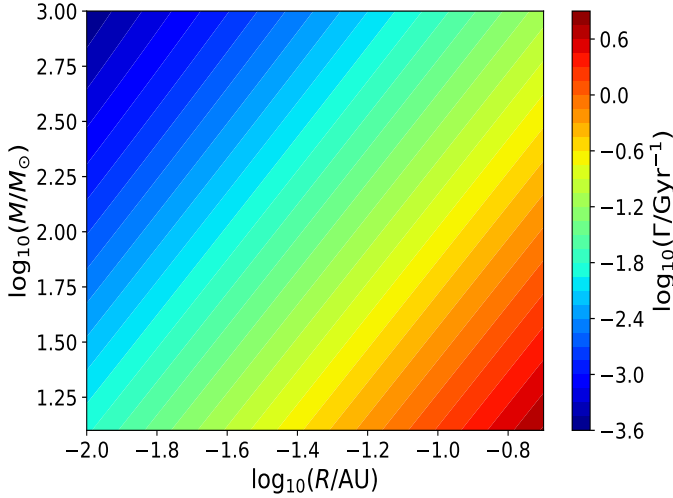


**Figure 9.** Collision rate of inner BBH and the flyby stars.  $M$  and  $R$  refer to the mass and semi-major axes of BBH, respectively.

Plugging the above results back into Eq. (9), we find that the collision rate of stars to BBH,  $\Gamma$ , depends on the BBH mass and semi-major as well as the distance from the center. To estimate  $\Gamma$ , we fix  $r = 6000 \text{ AU} = 0.03 \text{ pc} \approx 46.6 R_g$  and compute the collision rate as a function of the BBH mass and inner semi-major axes.

Figure 9 displays the behavior of  $\log_{10}(\Gamma/\text{Gyr}^{-1})$  as a function of the logarithm of BBH mass,  $\log_{10}(M/M_\odot)$  and logarithm of semi-major axes  $\log_{10}(R/\text{AU})$ . As expected, the rate enhances for larger/smaller BBH semi-major/mass, respectively.

## 8 LIFETIME OF ORBITS

Finally, we consider the lifetime of BBHs orbits under consideration. By the lifetime we mean the time that it takes for an inner binary with given initial parameters to merge. The above timescale is not meant to represent the detectability window. In Emami & Loeb (2020) we computed the rate for the inspiral of stellar mass BHs around the SMBH. Nonetheless the above timescale provides a sense about the lifetime of a given orbit under consideration. Binaries with very short lifetime do not survive. Their replenishment requires some secondary process after the merger such as gas supply (Secunda et al. 2019). On the other hand, binaries with long lifetime have a better chance of being seen in the real observations provided that they are not evaporated or tidally disrupted by the close flybys. Yet, since we are mostly interested in IMBHs with relatively large masses, the chance for a BBH to get destroyed by some dynamical interactions is not expected to be high. A comprehensive analysis of the rate of these binaries including the above effects goes beyond the scope of this paper.

Figure 10 presents the lifetime of BBHs for different values of their masses and as a function of  $e_{in}$  and  $a_{in}$ . For simplicity, we only focus on equal mass BHs. From the plot it is clear that the lifetime of the BBHs is a strong function of the orbital parameters as well as the BH masses. As ex-

pected, the lifetime increases by decreasing the values of  $e_{in}$  and increasing the value of  $a_{in}$ .

## 9 CONCLUSIONS

Multi-Wavelength GW detectors can monitor the spectrum of GW signals from the center of M87 over a wide range of frequencies and orbital parameters. GW spectroscopy enables one to reproduce the shape of the GW signal and get novel information about the physical process behind such signals. Focusing on triple systems in M87 made of an inner binary BHs with different masses, from stellar to IMBHs, we presented a consistent method for detecting GW signals by integrating over the observation time within the lifetime of different GW detectors. We demonstrated that the frequency peaks from various GW sources can be used to entangle the signal from closer in sources with continuum frequency bands. The parameter space where different GW detectors may overlap in their frequency of GWs, could be used as a novel way to break the degeneracy between different orbital parameters.

We estimated the rate of collision between the BBHs in M87 and the flyby stars belong to the stellar cluster at the central region of M87. Though the collision rate depends on the mass and the semi-major axes of inner binary, our results imply that the rate is smaller than  $10 \text{ Gyr}^{-1}$  for the wide range of parameters considered here.

A more detailed numerical simulation over a wider time range including all of the possible encounters between different BHs is left for a future investigation.

## ACKNOWLEDGEMENTS

We thank Bao-Minh Hoang, Bence Kocsis and Smadar Naoz for the thoughtful comments on the manuscript. We are thankful to Fabio Antonini, Evgeni Grishin and Scott A. Hughes for the interesting discussion. We are very grateful to an anonymous referee for their constructive comments that improved the quality of this paper. R.E. acknowledges the support by the Institute for Theory and Computation at the Center for Astrophysics. This work was also supported in part by the Black Hole Initiative at Harvard University which is funded by grants from the Templeton and Moore foundations. We thank the supercomputer facility at Harvard where most of the simulation work was done.

## REFERENCES

- Abbott B. P., et al., 2016a, *Phys. Rev. Lett.*, **116**, 061102
- Abbott B. P., et al., 2016b, *Phys. Rev. Lett.*, **116**, 241103
- Antonini F., Rodriguez C. L., Petrovich C., Fischer C. L., 2018, *MNRAS*, **480**, L58
- Antonini F., Gieles M., Gualandris A., 2019, *Monthly Notices of the Royal Astronomical Society*, **486**, 5008
- Arca Sedda M., et al., 2019, arXiv e-prints, p. arXiv:1908.11375
- Broderick A. E., Narayan R., Kormendy J., Perlman E. S., Rieke M. J., Doeleman S. S., 2015, *ApJ*, **805**, 179
- Bromm V., Larson R. B., 2004, *Annual Review of Astronomy and Astrophysics*, **42**, 79



# Probing Intermediate Mass Black Holes in M87 through Multi-Wavelength Gravitational Wave Observations

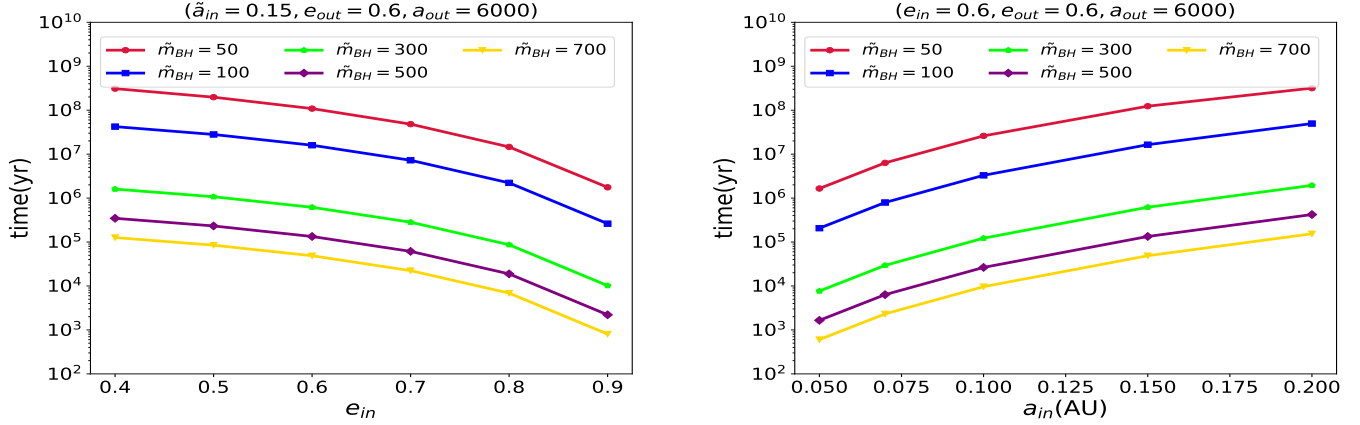


**Figure 10.** The lifetime of the BHs in the inner binary as a function of  $e_{in}$  (left) and  $a_{in}$  (right) and for different values of the BH masses.

Chilingarian I. V., Katkov I. Y., Zolotukhin I. Y., Grishin K. A., Beletsky Y., Boutsia K., Osip D. J., 2018, *The Astrophysical Journal*, **863**, 1

Devecchi B., Volonteri M., 2009, *The Astrophysical Journal*, **694**, 302

Emami R., Loeb A., 2019, arXiv e-prints, p. arXiv:1903.02579

Emami R., Loeb A., 2020, *J. Cosmology Astropart. Phys.*, **2020**, 021

Event Horizon Telescope Collaboration et al., 2019a, *The Astrophysical Journal*, **875**, L1

Event Horizon Telescope Collaboration et al., 2019b, *The Astrophysical Journal*, **875**, L2

Event Horizon Telescope Collaboration et al., 2019c, *The Astrophysical Journal*, **875**, L3

Event Horizon Telescope Collaboration et al., 2019d, *The Astrophysical Journal*, **875**, L4

Event Horizon Telescope Collaboration et al., 2019e, *The Astrophysical Journal*, **875**, L5

Event Horizon Telescope Collaboration et al., 2019f, *The Astrophysical Journal*, **875**, L6

Fragione G., Grishin E., Leigh N. W. C., Perets H. B., Perna R., 2019, *MNRAS*, **488**, 47

Gebhardt K., Thomas J., 2009, *The Astrophysical Journal*, **700**, 1690

Gebhardt K., Adams J., Richstone D., Lauer T. R., Faber S. M., Gültekin K., Murphy J., Tremaine S., 2011, *The Astrophysical Journal*, **729**, 119

Ghez A. M., Klein B. L., Morris M., Becklin E. E., 1998, *The Astrophysical Journal*, **509**, 678

Giersz M., Leigh N., Hypki A., Lützgendorf N., Askar A., 2015, *MNRAS*, **454**, 3150

Gravity Collaboration et al., 2018, *Astronomy and Astrophysics*, **618**, L10

Greene J. E., et al., 2019, arXiv e-prints, p. arXiv:1903.08670

Grishin E., Perets H. B., Zenati Y., Michaely E., 2017, *MNRAS*, **466**, 276

Grishin E., Perets H. B., Fragione G., 2018, *MNRAS*, **481**, 4907

Hoang B.-M., Naoz S., Kocsis B., Rasio F. A., Dosopoulou F., 2018, *ApJ*, **856**, 140

Hoang B.-M., Naoz S., Kocsis B., Farr W. M., McIver J., 2019, *The Astrophysical Journal*, **875**, L31

Johnson J. L., Haardt F., 2016, *Publications of the Astronomical Society of Australia*, **33**, e007

Kocsis B., Levin J., 2012, *Physical Review D*, **85**, 123005

Leigh N. W. C., Lützgendorf N., Geller A. M., Maccarone T. J., Heinke C., Sesana A., 2014, *MNRAS*, **444**, 29

Leigh N. W. C., Antonini F., Stone N. C., Shara M. M., Merritt D., 2016, *MNRAS*, **463**, 1605

Leigh N. W. C., et al., 2018, *MNRAS*, **474**, 5672

Loeb A., Rasio F. A., 1994, *The Astrophysical Journal*, **432**, 52

Madau P., Rees M. J., 2001, *The Astrophysical Journal*, **551**, L27

Mapelli M., 2016, *Monthly Notices of the Royal Astronomical Society*, **459**, 3432

McKernan B., Ford K. E. S., Lyra W., Perets H. B., 2012, *MNRAS*, **425**, 460

McKernan B., Ford K. E. S., Kocsis B., Lyra W., Winter L. M., 2014, *MNRAS*, **441**, 900

Mezcua M., 2017, *International Journal of Modern Physics D*, **26**, 1730021

Mezcua M., Civano F., Marchesi S., Suh H., Fabbiano G., Volonteri M., 2018, *Monthly Notices of the Royal Astronomical Society*, **478**, 2576

Miller M. C., Colbert E. J. M., 2004, *International Journal of Modern Physics D*, **13**, 1

Murphy J. D., Gebhardt K., Adams J. J., 2011, *ApJ*, **729**, 129

Naoz S., Silk J., 2014, *ApJ*, **795**, 102

Naoz S., Kocsis B., Loeb A., Yunes N., 2013, *The Astrophysical Journal*, **773**, 187

Natarajan P., 2014, *General Relativity and Gravitation*, **46**, 1702

Pan T., Loeb A., 2012, *MNRAS*, **425**, L91

Peters P. C., Mathews J., 1963, *Physical Review*, **131**, 435

Portegies Zwart S. F., Makino J., McMillan S. L. W., Hut P., 1999, *Astronomy and Astrophysics*, **348**, 117

Randall L., Xianyu Z.-Z., 2019, arXiv e-prints, p. arXiv:1902.08604

Reines A., Condon J., Darling J., Greene J., 2019, arXiv e-prints, p. arXiv:1909.04670

Remillard R. A., McClintock J. E., 2006, *Annual Review of Astronomy and Astrophysics*, **44**, 49

Robson T., Cornish N. J., Liu C., 2019, *Classical and Quantum Gravity*, **36**, 105011

Rodriguez C. L., Antonini F., 2018, *ApJ*, **863**, 7

Secunda A., Bellovary J., Mac Low M.-M., Ford K. E. S., McKernan B., Leigh N. W. C., Lyra W., Sándor Z., 2019, *ApJ*, **878**, 85

Sesana A., et al., 2019, arXiv e-prints, p. arXiv:1908.11391

Walker C., Davies F., Wrobel J., Junor B., Ly C., Hardee P., 2009, in *New Science Enabled by Microarcsecond Astrometry*. p. P3

Walsh J. L., Barth A. J., Ho L. C., Sarzi M., 2013, *The Astrophysical Journal*, **770**, 86

Wang F., et al., 2015, *ApJ*, **807**, L9

Webster B. L., Murdin P., 1972, *Nature*, **235**, 37

This paper has been typeset from a  $\text{\TeX}/\text{\LaTeX}$  file prepared by the author.